Electronic Supplementary Information

for

Promoting CO_2 electroreduction activity of porphyrinic conjugated microporous polyanilines via accelerating proton transfer dynamics

Feng Qiu,[a] Chunyan Li,[a] Xiaodong Xuan,[a] Senhe Huang,[b] Chenbao Lu,*[b]

Hualin Lin,[a] Sheng Han,*[a] Xiaodong Zhuang[b] Wai-Yeung Wong*[c]

[a] School of Chemical and Environmental Engineering, Shanghai Institute of Technology, 100 Haiquan Road, Shanghai 201418, P. R. China.

[b] The Meso-Entropy Matter Lab, State Key Laboratory of Metal Matrix Composites & Shanghai Key Laboratory of Electrical Insulation and Thermal Ageing, Frontiers Science Center for Transformative Molecules, School of Chemistry and Chemical Engineering, Shanghai Jiao Tong University, 800 Dongchuan Road, Shanghai 200240, P. R. China.

[c] Department of Applied Biology and Chemical Technology and Research Institute for Smart Energy, The Hong Kong Polytechnic University, Hung Hom, Hong Kong, P. R. China.

Corresponding Author

Chenbao Lu: E-mail: castle@sjtu.edu.cn

Sheng Han: E-mail: hansheng654321@sina.com

Wai-Yeung Wong: E-mail: wai-yeung.wong@polyu.edu.hk

Table of Contents

1. Experiments and characterization

1.1 Chemicals

All organic solvents were purchased from Titan and used without purification. Acetic acid, nitrobenzene, 2-(dicyclohexylphosphino)-2,4,6-triisopropylbiphenyl (XPhos), bis(dibenzylideneacetone)palladium ($Pd(dba)_2$), p-bromobenzaldehyde, potassium tert-butoxide (t-BuOK) and cobalt acetate were purchased from Titan Scientific Co., Ltd. and used as received. Pyrrole was purified by distilling under reduced pressure. 5,10,15,20-tetrakis(4'-bromophenyl) cobalt(II) porphyrin (4Br-CoPor) was synthezied accroding to the previous work.[1]

1.2 Synthesis of Cobalt(II) 5,10,15,20-tetrakis(4'-bromophenyl)porphyrin (4Br-CoPor)

p-Bromobenzaldehyde (3.72 g, 20 mmol) was dissolved in nitrobenzene (100 mL) and acetic acid (150 mL), then the freshly distilled pyrrole (1.4 mL, 20 mmol) was added. The mixture was stirred at 120 °C for 1 hour and then cooled to room temperature. The resulting dark purple precipitate was collected by filtration and washed with methanol (50 mL × 3). The crude product was purified by column chromatography eluting with dichloromethane to obtain the target product as a purple crystalline powder (1.92 g) with yield of 42%. 1H NMR ($CDCl_3$, 500 MHz): δ (ppm) = -2.84 (s, 2H, NH), 7.91-7.94 (d, 8H, $CH_{Ar\text{-}phenyl}$), 8.06-8.09 (d, 8H, $CH_{Ar\text{-}phenyl)}$, 8.84 (s, 8H, $CH_{pyrrole}$). Then, the product (1.92 g, 2.06 mmol) and cobalt acetate (3.65 g, 20.64 mmol) were dissolved in 200 mL of DMF and refluxed at 150 °C for 8 h. The resulting solution was cooled to room temperature, an appropriate amount of deionized water was added, the precipitate was filtered, washed three times with deionized water, and the crude product was purified by silica gel column chromatography with dichloromethane as the eluent to obtain the target compound (1.4 g, 68%). MALDI–TOF MS (m/z): Calculated for $C_{44}H_{24}Br_4CoN_4$: 987.253. Found: 986.782.

1.3 Synthesis of CMPANIs

In the glove box, 4Br-CoPor (247 mg, 250 μmol), diamino monomers (500 μmol), $Pd(dba)_2$ (15 mg, 26 μmol), XPhos (19 mg, 39 μmol) and potassium tert-butoxide (149 mg, 1.33 mmol) was mixed and dissolved in 15 mL of dioxane in

a Schlenk tube. These mixtures were stirred at 105 ^{o}C for 3 days. The products were further purified by Soxhlet extraction with dichloromethane, THF, and acetone, respectively. After drying in a vacuum oven overnight, a black solid was obtained with yield of 75-90%.

1.4 Characterization

^{1}H nuclear magnetic resonance (NMR) spectroscopy was measured on a Bruker 500 (500 MHz for proton) spectrometer (Bruker, Karlsruhe, Germany) with tetramethylsilane as the internal reference, using $CDCl_3$ as solvent. Matrix-Assisted Laser Desorption/Ionization Time of Flight mass spectrometry (MALDI-TOF) was performed on autoflex speed TOF/TOF (Bruker, Karlsruhe, Germany). Fourier-transform infrared spectroscopy (FTIR) was recorded with a Spectrum 100 spectrometer (Perkin Elmer, Spectrum 100). X-ray photoemission spectroscopy (XPS) measurements were performed on a PHI–5000C ESCA system, the C 1s value was set at 284.8 eV for charge corrections. Thermogravimetric analysis (TGA) was performed on a Q5000IR thermogravimetric analyzer (TA Instruments, USA) to investigate the thermal stability of all samples in a N_2 atmosphere from ambient temperature to 800 ^{o}C increasing at 20 ^{o}C min^{-1}. Pd content was determined by inductively coupled plasma mass spectrometry (ICP-MS). Firstly, the sample (25 mg) was digested in the mixture of HNO_3 (0.8 mL/) and H_2O_2 (0.2 mL) at 60 °C for 12 h, then it cooled to room temperature and diluted with HNO_3 (4 mL). The samples were analysed by ICP-MS (Perkin Elmer NexION 2000G). The physisorption isotherms were measured via an Auto-sorb-iQA3200-4 sorption analyzer (Quantatech Co., USA) based on N_2 adsorption/desorption at 77 K. CO_2 adsorption/desorption isotherms at 273 and 298 K were conducted on a Quantachrome Autosorb-1MP instrument. The specific surface areas were calculated by applying the Brunauer−Emmett−Teller (BET) model to adsorption or desorption branches of the isotherms using the QuadraWin 5.05 software package. XRD analysis was performed on a RigakuD/Max 2500 X-ray diffractometer with Cu Ka radiation (k=1.54 Å) at voltage of 40 kV and a generator current of 50 mA with a scanning speed of 6° min^{-1} over the range of 5-60°. Scanning electron microscopy (SEM) was performed using an FEI Sirion-200 field-emission scanning electron microscope (FEI Co., USA). Transmission electron microscopy (TEM) was performed with a Tecnai G2 F20

S-TWIN instrument operated at 200 kV. Ultraviolet-Visible (UV-vis) spectra were recorded on a Lambda 950 UV-VIS-NIR spectrophotometer by using a 10 mm optical-path quartz cell at room temperature. Ultraviolet photoemission spectroscopy (UPS) was conducted on a Kratos AXIS Ultra-DLD Photoelectron Spectrometer under an ultrahigh vacuum of about 3×10^{-9} Torr with an unfiltered He I gas discharge lamp source (21.22 eV) at 300 K. XANES and EXAFS measurements were tested on the BL10C beam line of Pohang light source 110.

1.5 H-type electrochemical measurements

The electrocatalytic CO_2 reduction was performed in a three electrode H-type cell, in which Ag/AgCl acts as the reference electrode, Pt plate as the counter electrode, and catalysts loaded on carbon paper as the working electrode. For preparation of working electrodes, typically, 1 mg of catalysts and 9 mg commercial carbon nanotubes were blended with 1 mL of Nafion solution (0.5 wt. %, DuPont, Ltd.) and the mixture was stirred for 12 h to ensure uniform mixing the catalyst ink. Then 100 μL of the catalyst ink was pipetted onto the carbon paper surface (1 cm^2), giving a catalyst loading of 0.1 mg cm^{-2}. All potentials reported in this work were referenced to reversible hydrogen electrode (RHE) using the following formula:

$$E_{RHE}\,(V) = E_{Ag/AgCl}\,(V) + 0.197\ (V) + 0.0591\ (V) \times pH \quad \cdots\cdots\cdots\cdots\cdots\cdots \quad \text{eq S1}$$

The electrolyte was CO_2 saturated 0.5 M $KHCO_3$, and CO_2 (Air Liquid, Ltd.) was continuously supplied to the cell (20 mL min^{-1}) through a gas bubbling tube during the constant potential electrolysis. The LSV curves were obtained with a scan rate of 5 mV s^{-1}, all potentials in this study were without iR compensation. The electrochemical double-layer capacitances (C_{dl}) of catalysts were calculated from CV curves. The CV curves were performed at scan rates varying from 10 to 100 mV s^{-1} in the region from −0.7 to −0.9 V. The capacitive currents of ΔJ ($J_{anodic} - J_{cathodic)}$ are plotted as a function of the CV against the scan rate. The slope of the fitting line is equal to twice the C_{dl}, which is linearly proportional to the electrochemically effective surface area of the electrode. The gaseous products were monitored by an online gas chromatography (GC, Shimadzu GC-2014C), equipped with a thermal conductivity detector (TCD) for H_2 and a flame ionization detector (FID) for CO quantification. A GC run repeats

every 18 minutes. The GC was calibrated with standard gas mixtures (Air Liquide, CO, H_2, CH_4, C_2H_4, C_2H_6, C_2H_2 in N_2) before the product measurements. The liquid products in the $KHCO_3$ solution were analyzed and quantified through a Bruker 500 MHZ (AVANCE III) NMR spectrometer with water suppression. After electrolysis, $KHCO_3$ electrolyte (0.5 mL) was collected and mixed with D_2O (0.1 mL) in an NMR tube using dimethyl sulfoxide (DMSO, 0.05 μL) as an internal standard.

1.6 Flow cell electrochemical measurements

Electrochemical reduction of CO_2 was performed in a flow-cell set-up with three chambers. An anion exchange membrane (FAB-PK-130, Fuel Cell Store, 1 × 1 cm^2) was used to separate the anode and cathode chambers, Hg/HgO electrode was used as the reference electrode, platinum network (1 × 1 cm^2) was used as the counter electrode, catalysts loaded on gas diffusion electrode (0.1 mg cm^{-2}, 1 × 1 cm^2) was used as the working electrode; 1 M KOH aqueous solution was used as the electrolyte, the electrolyte was circulated through the cathode and anode chambers at a rate of 20 mL min^{-1} by two peristaltic pumps. Pure CO_2 gas (99.999%) was continuously supplied to the gas chamber at a flow rate of 10 mL min^{-1}.

1.7 Faradic efficiency (FE) calculation

Faradaic Efficiency (FE) of CO and H_2 were calculated via the following equation:

$$FE = \frac{Q_i}{Q_{total}} = \frac{2 \times P_0 \times F \times v \times v_i}{R \times T \times I} \quad \cdots\cdots\cdots\cdots\cdots\cdots \text{ eq S2}$$

where Q_i is the quantity of electric charge needed to produce the corresponding product i. Q_{total} is the quantity of electric charge needed to produce all products. 2 is the number of electrons transferred per mole CO_2 to CO or per mole H_2O to H_2. P_0 is the atmospheric pressure (1.01 × 10^5 Pa), F is the faradaic constant (96485 C mol^{-1}), v is the gas flow rate measured by flow meter, v_i is the volume concentration of gas product in the exhaust gas from the cell determined by online GC. T is the reaction temperature (298.15 K), R is the ideal gas constant (8.314 J mol^{-1} K^{-1}), and I is the current at each potential.

1.8 Evaluation of turnover frequency (TOF)

The TOF (h^{-1}) of product CO was evaluated as follows:

$$\text{TOF} = \frac{FE_{CO} \times j_{total} \times A \times M_{Co} \times t}{n \times F \times \omega_{Co} \times m} \quad \cdots\cdots\cdots\cdots \text{eq S3}$$

where FE is the faradaic efficiency of CO, j is the total current density, A (1 cm^2) is the electrode geometric area, ω_{Co} is the mass fraction of cobalt on the catalyst obtained by ICP-MS measurement, m is the mass of catalyst coated on working electrode, and M_{Co} is the atomic mass of Co (59 g mol^{-1}). F is the faradaic constant (96485 C mol^{-1}), t is the reaction time (1 h/3600 s), n is the number of electrons transferred for product formation, which is 2 for CO.

1.9 DFT Calculations

Electronic properties (HOMO-LUMO) of porphyrin molecules were performed using the Gaussian 09 program. A PBE0 functional with D3 correction (Becke–Johnson damping) was adopted for its robustness and dispersion corrections, which make it widely accepted as the proper functional to study the reactions of transition metal complexes. The Stuttgart–Dresden pseudopotential and double-ξ valence basis set were used for transition metal atoms (cobalt). For all other main group elements (H, C, N, O), the all-electron 6–31G* basis set was used. The geometric structures of all species were fully optimized.

The free energy calculations were performed using the Vienna *ab* initio simulation package (VASP) with the projector-augmented wave (PAW) method. All calculations were based on the same generalized gradient approximation (GGA) method with Perdew-Burke-Ernzerhof (PBE) functional for the exchange-correlation term. The plane wave cutoff was set to 400 eV. The Brillouin zone integration was carried out with 1×1×1 Monkhorst-Pack *k*-point grid. The cells of molecules were built with vacuum slab height of 10 Å along x, y and z direction. The convergence of energy and forces were set to 5×10^{-7} eV and 0.001 eV $Å^{-1}$ for structure optimization, respectively.

The CRR pathway with CO production can be summarized as follows:

Overall: $CO_2 + 2H^+ + 2e^- \rightarrow CO + H_2O$

$CO_2 + * + H^+ + e^- \rightarrow COOH^*$, ΔG_1

$COOH^* + H^+ + e^- \rightarrow CO^* + H_2O$, ΔG_2

$CO^* \rightarrow CO + *$ ΔG_3

The free energy of the adsorption of intermediates including COOH* and CO* was calculated by: $G = E^{DFT} + ZPE - T\Delta S$, where E^{DFT} is the DFT-optimized total energy, ZPE is the zero-point vibrational energy, T is the temperature, and ΔS is the entropy). The zero-point energies and entropies of the reaction species were calculated from the vibrational frequencies.

2. Figures

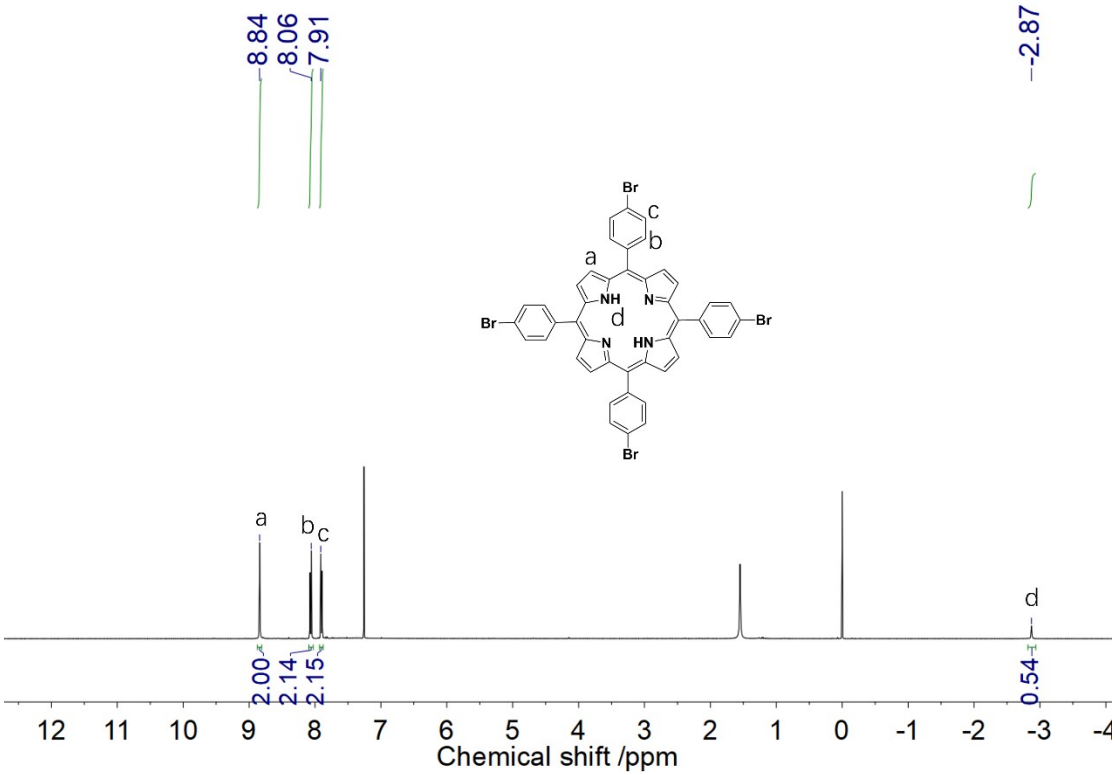

Fig. S1 ^{1}H NMR spectrum of 4Br-Por in $CDCl_3$.

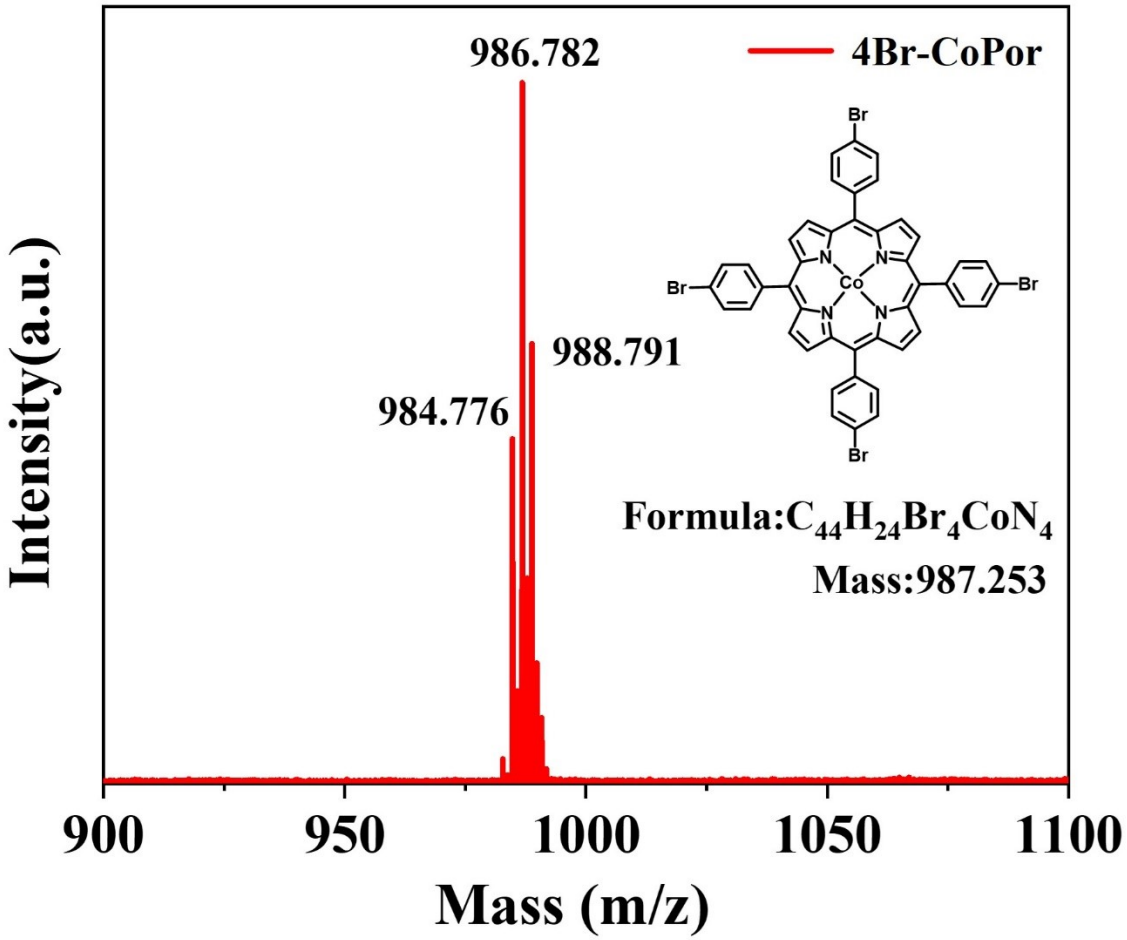

Fig. S2 The MALDI-TOF mass spectrum of 4Br-CoPor.

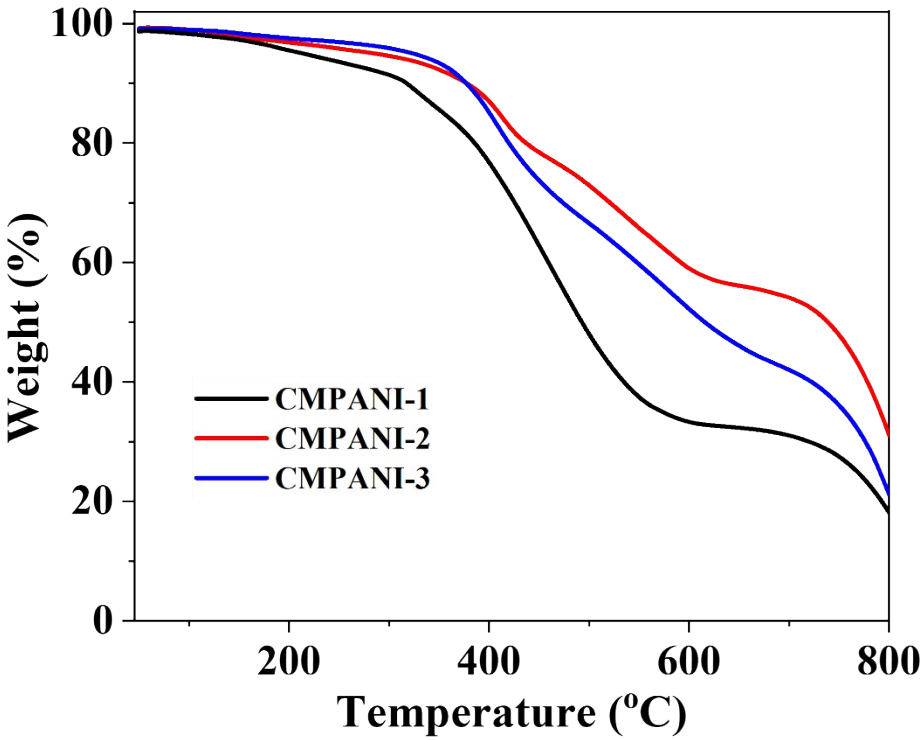

Fig. S3 The TGA curves of CMPANI-n

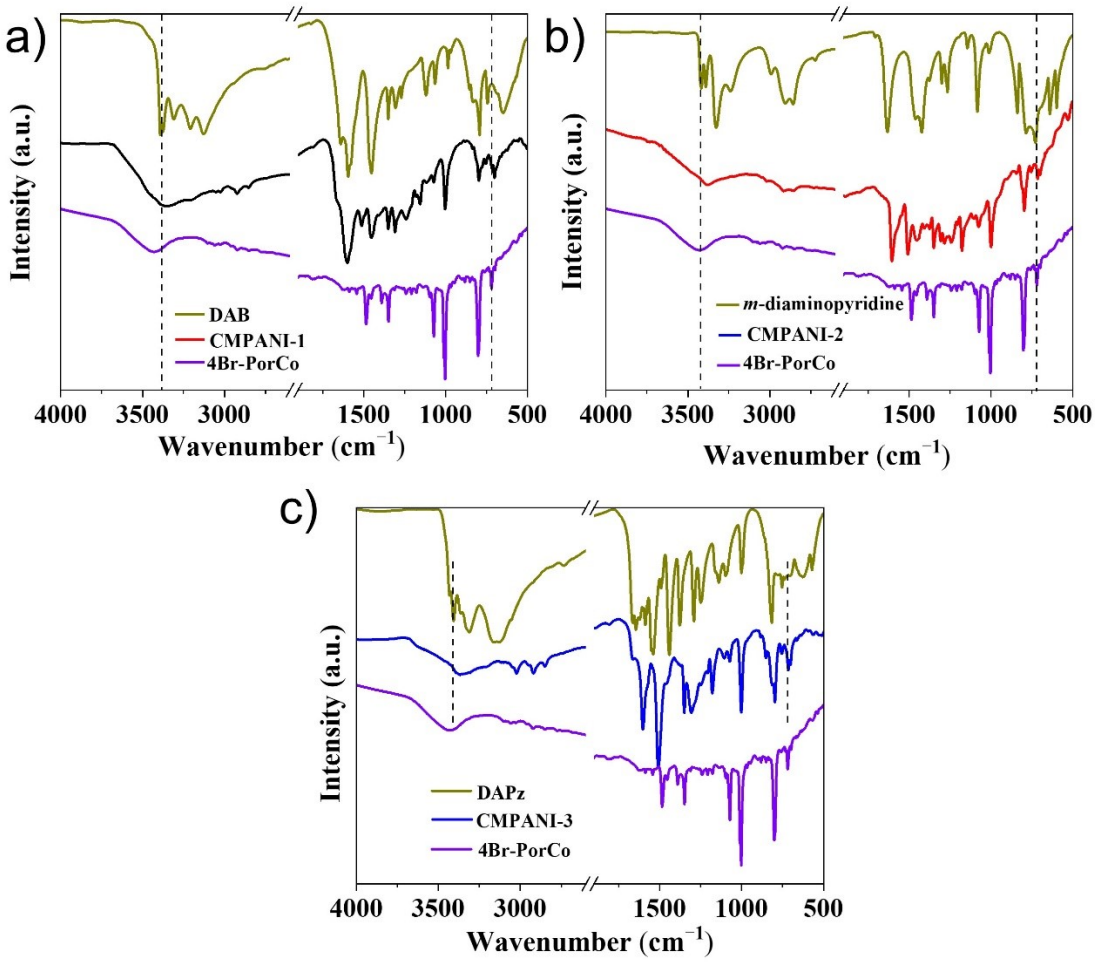

Fig. S4 The comparison of CMPANI-n with their precursors. The FTIR spectra of CMPANI-1 (a), CMPANI-2 (b), and CMPANI-3 (c)

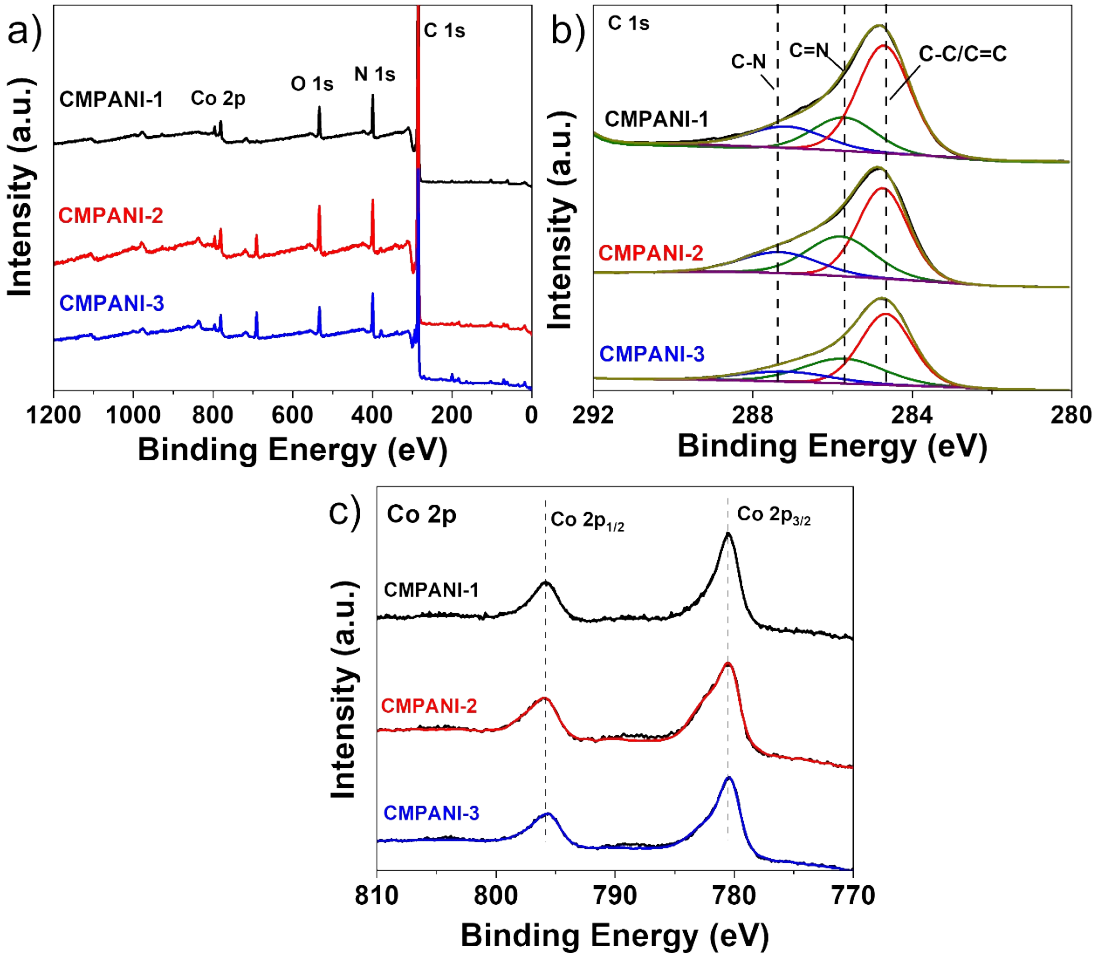

Fig. S5. (a) XPS spectra of CMPANI-n; (b) The high resolution of C 1s XPS spectra of CMPANI-n; (c) The high resolution of Co 2p XPS spectra of CMPANI-n.

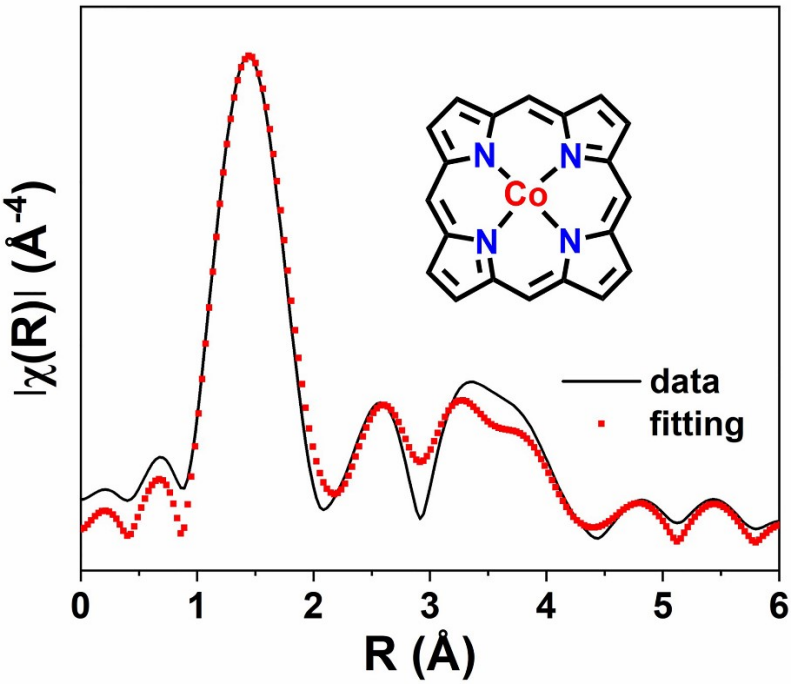

Fig. S6 Fitting of Fourier transformation of EXAFS spectra for CMPANI-3 (black: experimental result, red: fitting line), the main peak appears at ~1.44 Å can be assigned to Co-N first shell in CoPor structure.

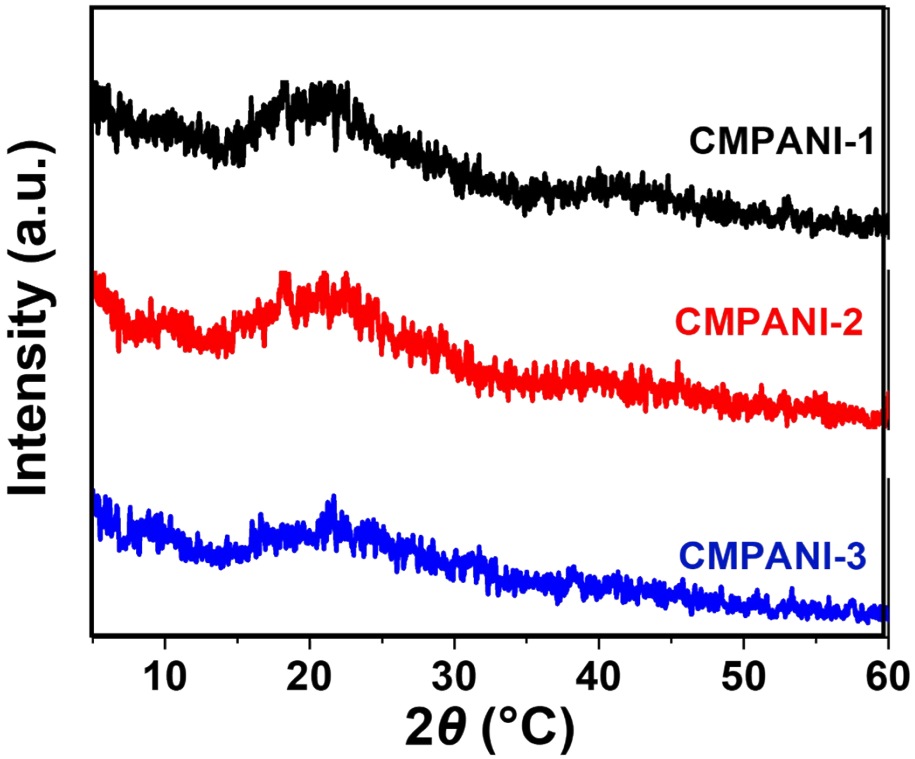

Fig. S7 XRD curves of CMPANI-n

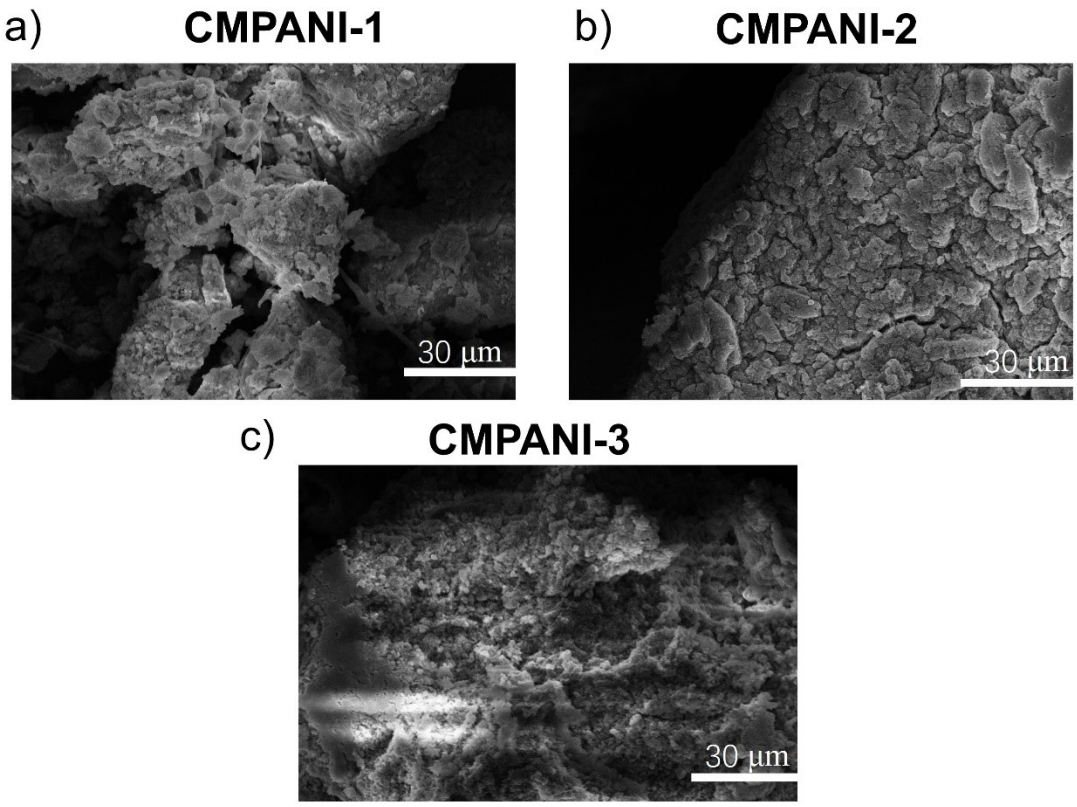

Fig. S8 SEM images of CMPANI-1 (a), CMPANI-2 (b), and CMPANI-3 (c).

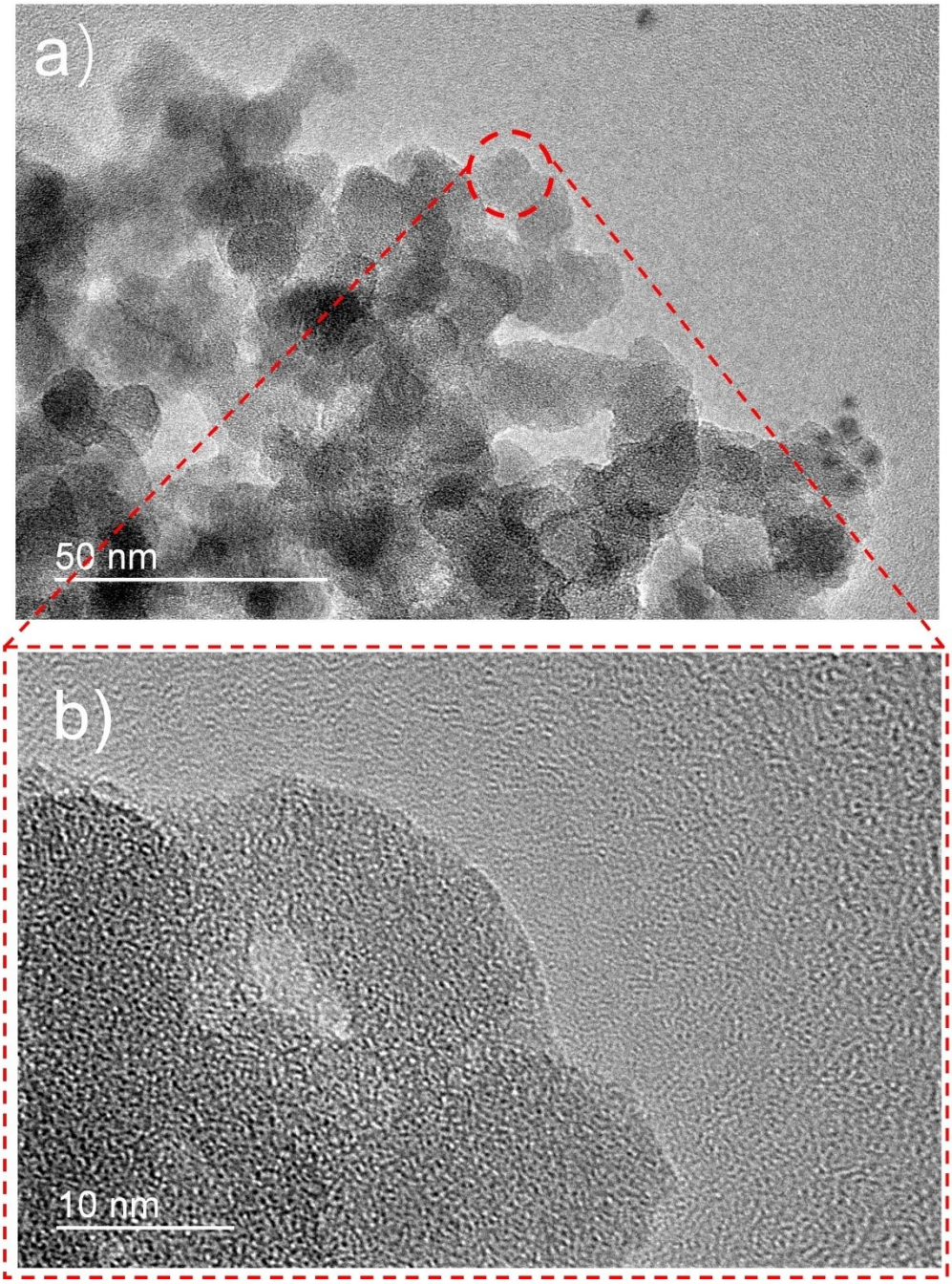

Fig. S9 TEM image for CMPANI-3

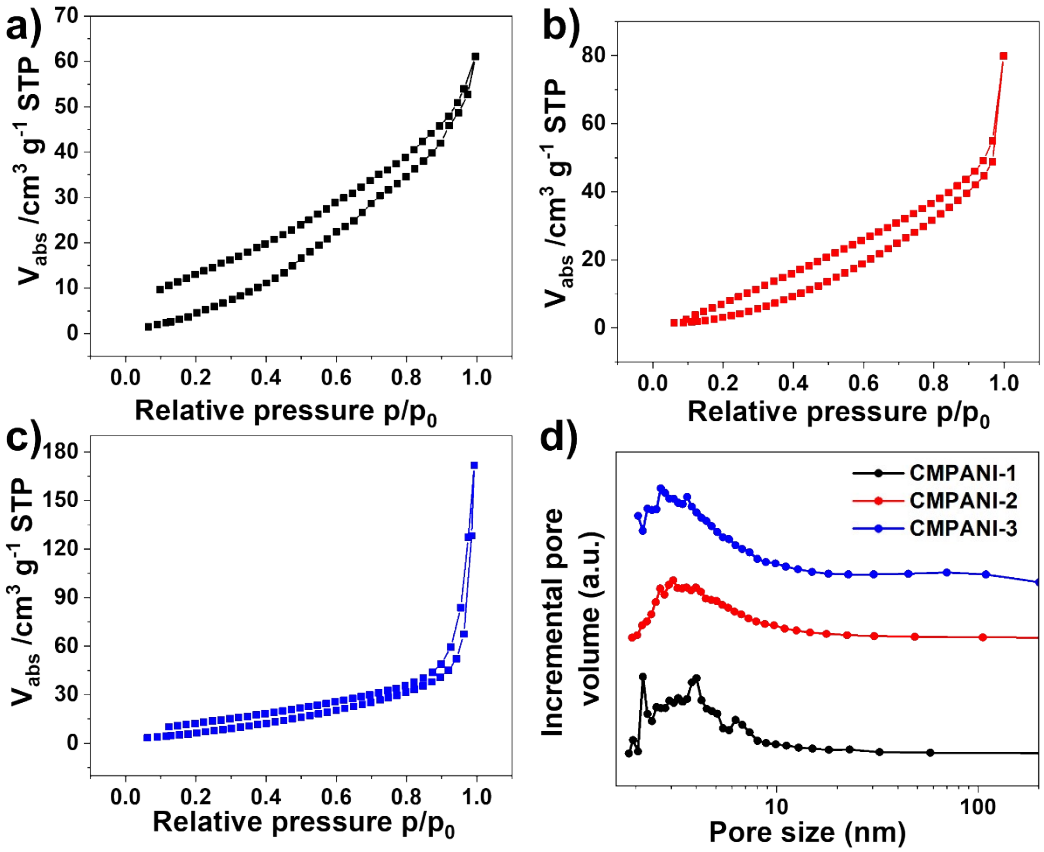

Fig. S10 a) Nitrogen adsorption/ desorption isotherms of a) CMPANI-1, b) CMPANI-2, c) CMPANI-3 at 77 K; d) pore size distribution for CMPANI-n obtained from analysis of the N_2 adsorption data.

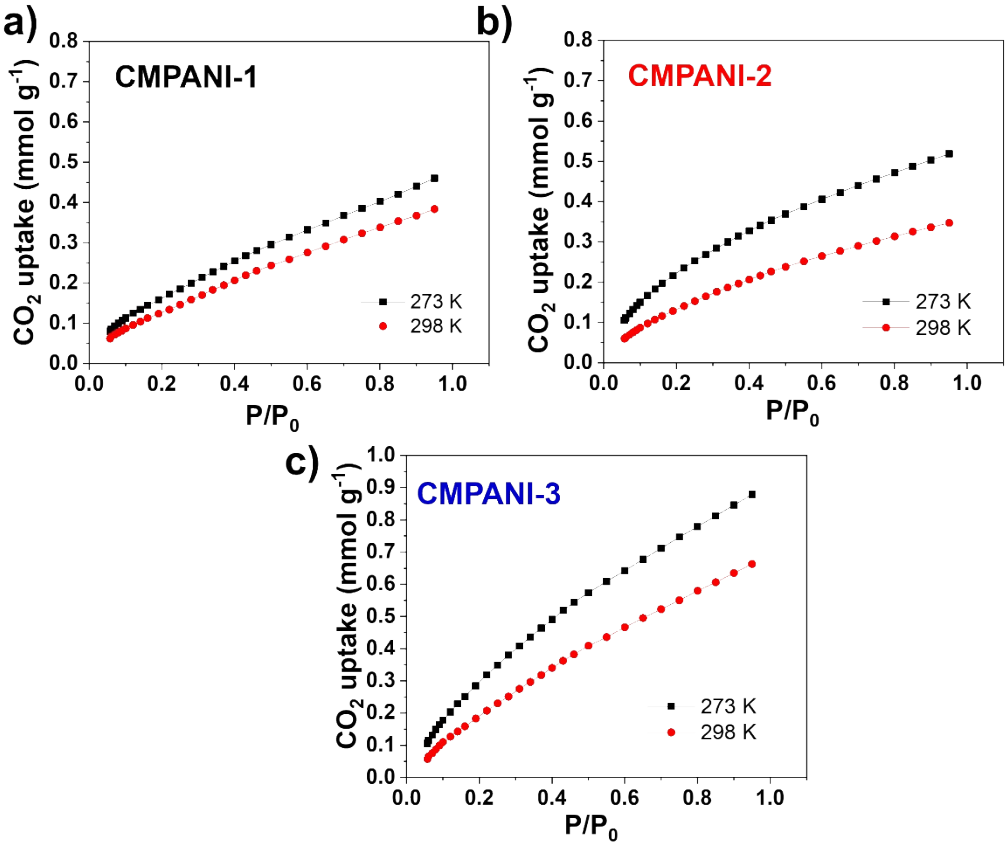

Fig. S11 CO_2 adsorption isotherms of CMPANI-n at 273 and 298 K, respectively.

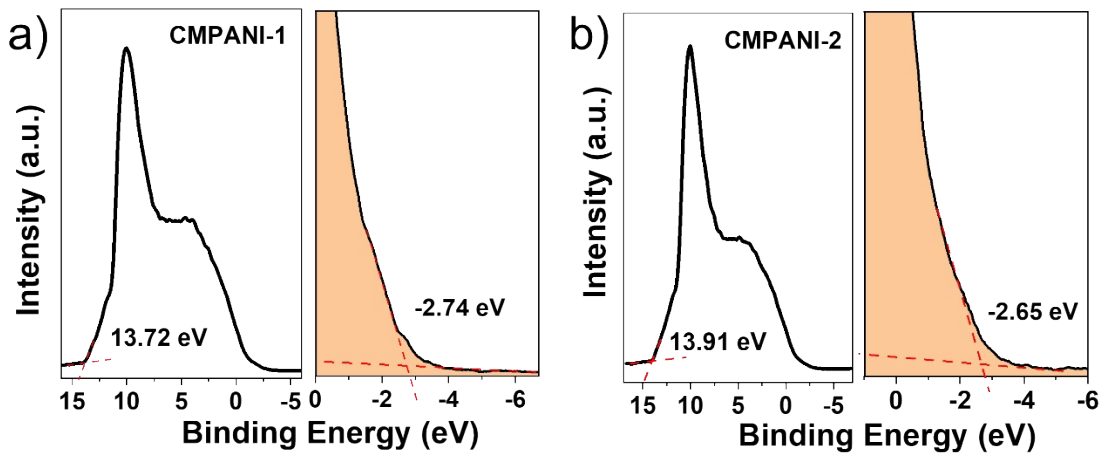

Fig. S12 UPS spectra of (a) CMPANI-1, and (b) CMPANI-2.

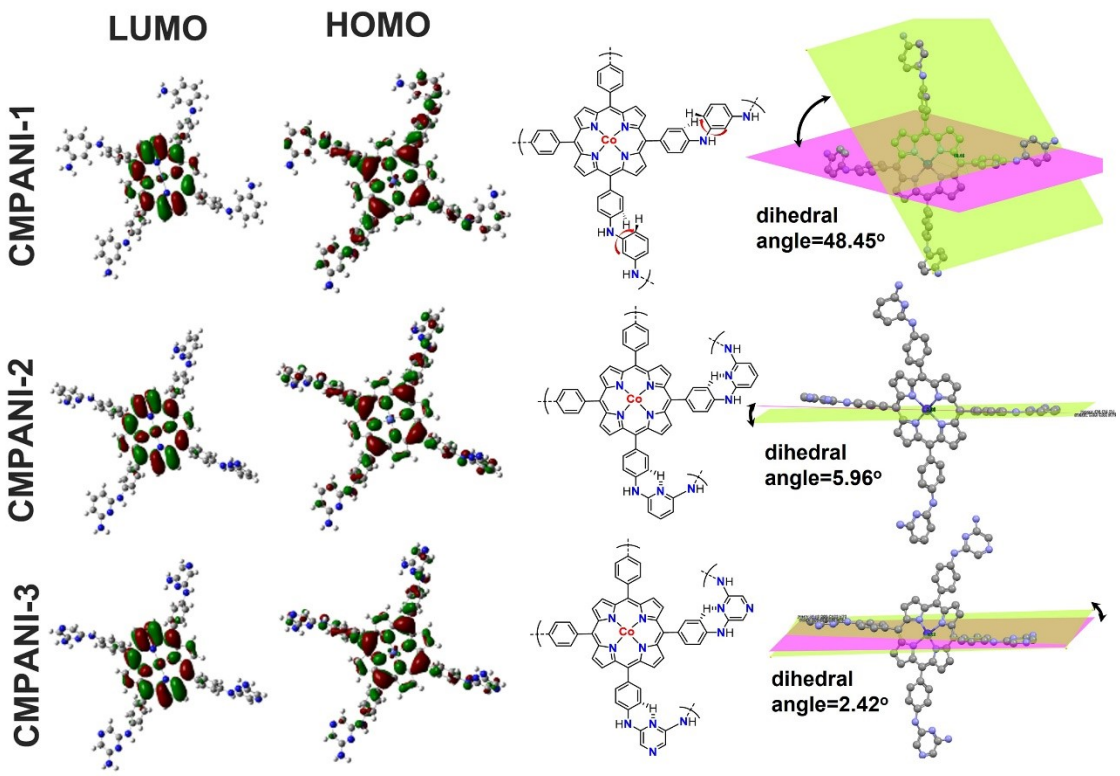

Fig. S13 Calculated HOMO and LUMO levels and the structures of CMPANI-n.

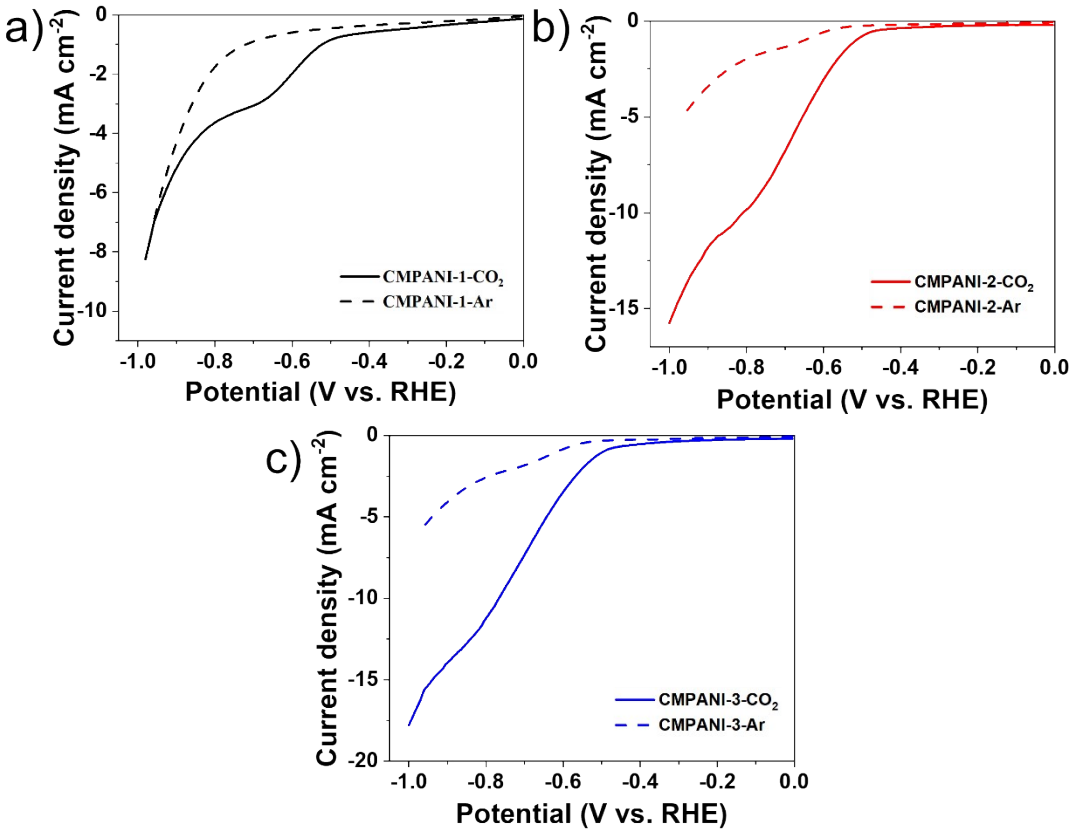

Fig. S14 The linear sweep voltammetry (LSV) curves of (a) CMPANI-1, (b) CMPANI-2, and (c) CMPANI-3 in Ar and CO_2 saturated solution

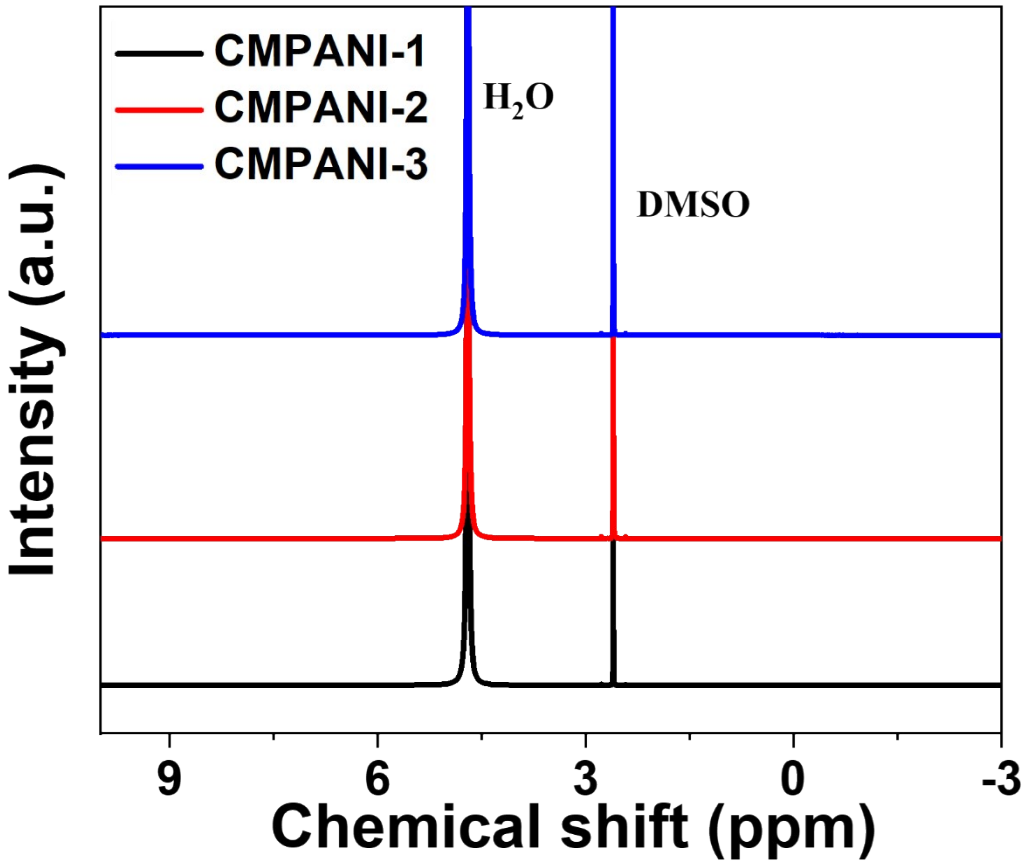

Fig. S15 ^{1}H NMR spectra of product (potential with −0.7 V) using CMPANI-1, CMPANI-2, and CMPANI-3.

Only the water and solvent signals were found, which indicates that no additional liquid products were generated during the CO_2RR reaction.

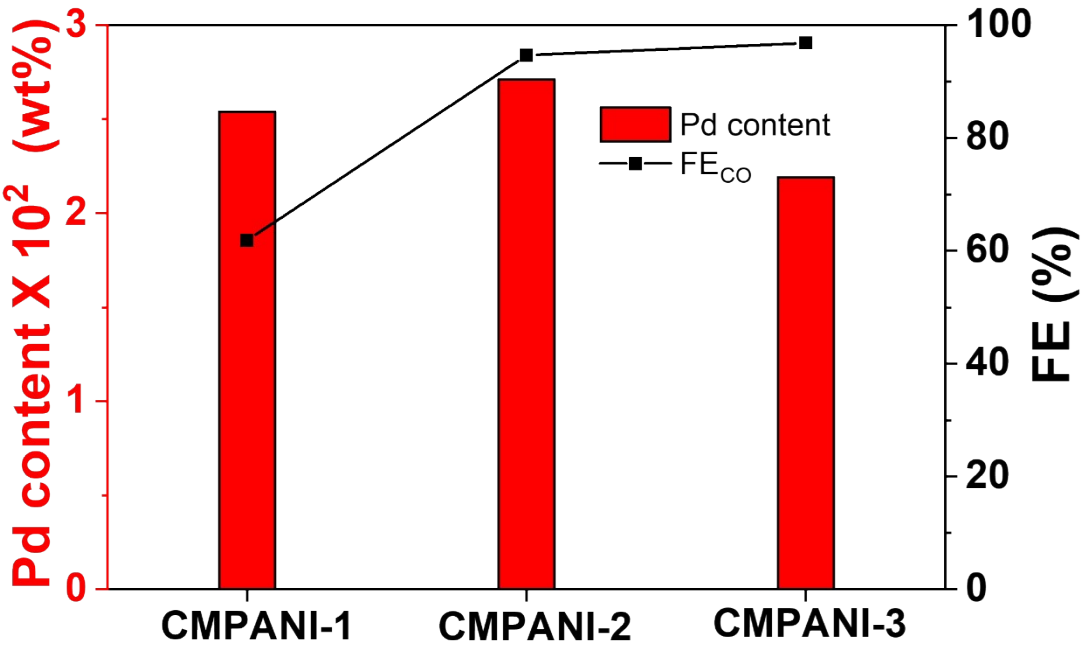

Fig. S16 comparing palladium content with the rate of CO formation in CMPANI-n.

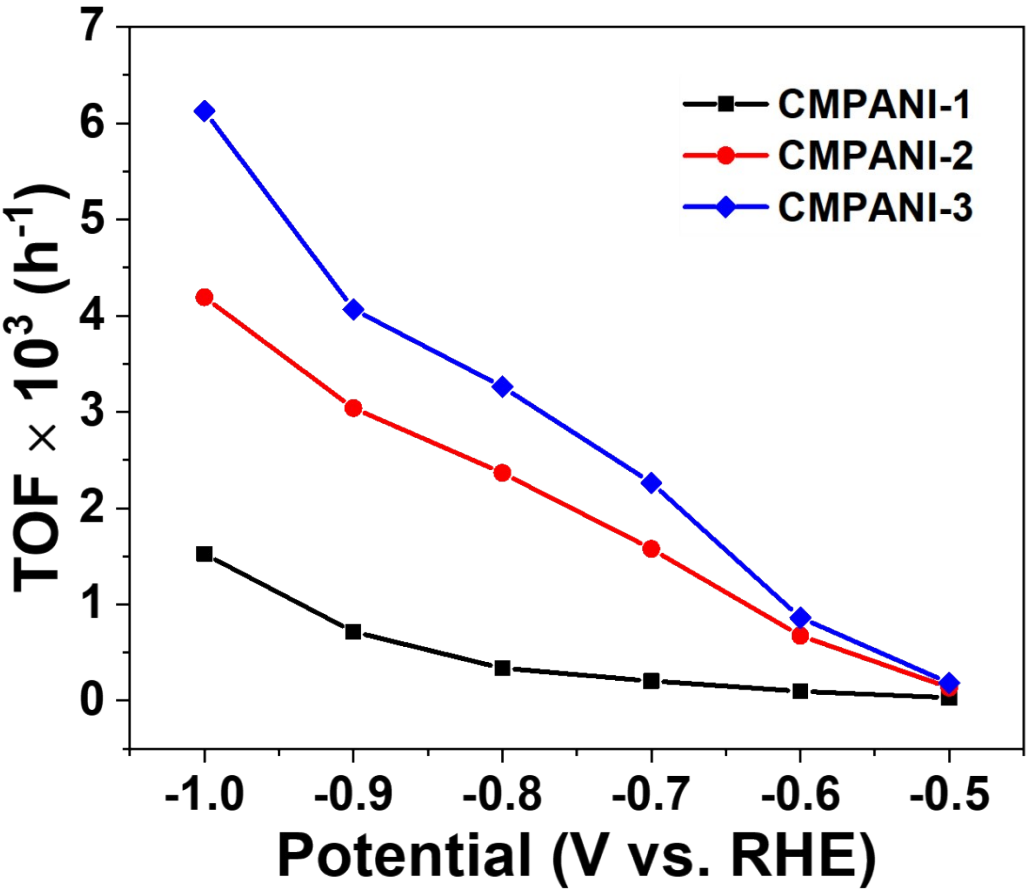

Fig. S17 The Turnover Frequency of CMPANI-n.

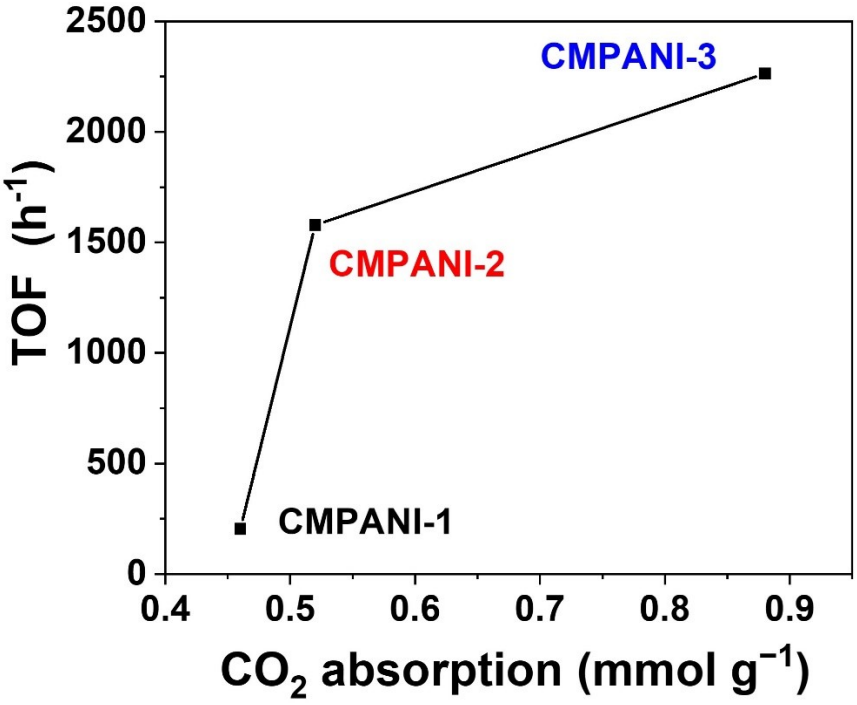

Fig. S18 comparing ability of CO_2 absorption with the TOF values in CMPANI-n

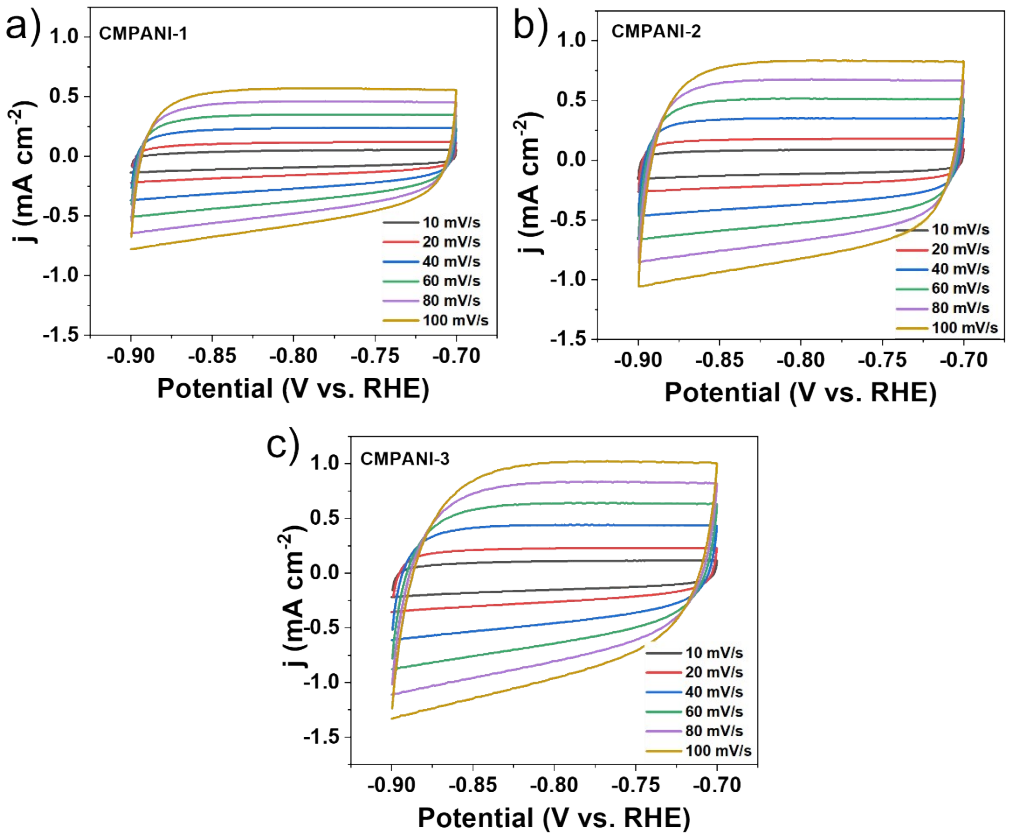

Fig. S19 Cyclic voltammetry measurements were then performed at scan rates varying from 10 to 100 mV s^{-1}. (a) CV curves for CMPANI-1; (b) CV curves for CMPANI-2; (c) CV curves for CMPANI-3.

a)

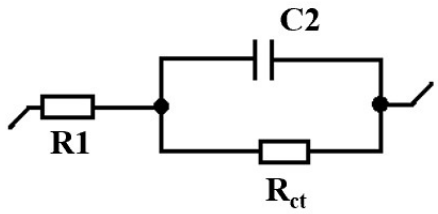

b)

Samples	R_{ct}
CMPANI-1	37.15
CMPANI-2	32.71
CMPANI-3	31.89

Fig. S20 (a) Equivalent circuit used for the fitting of EIS data; (b) The calculated R_{ct} values of CMPANI-n.

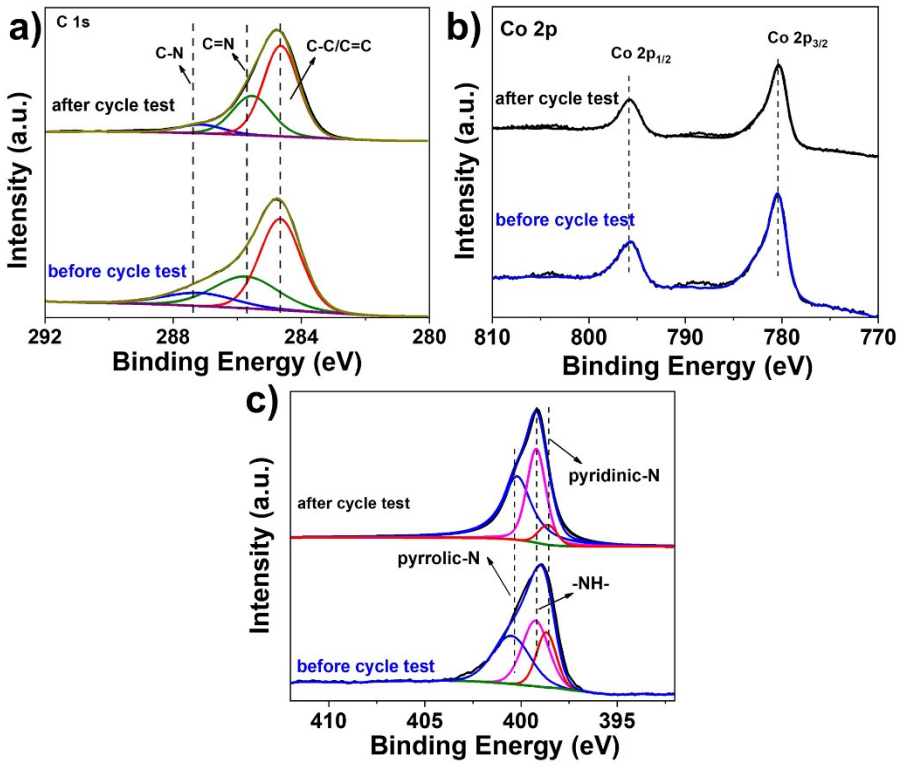

Fig. S21 (a) C 1s, (b) Co 2p and (c) N 1s XPS spectra of CMPANI-3 before and after cycle stability test.

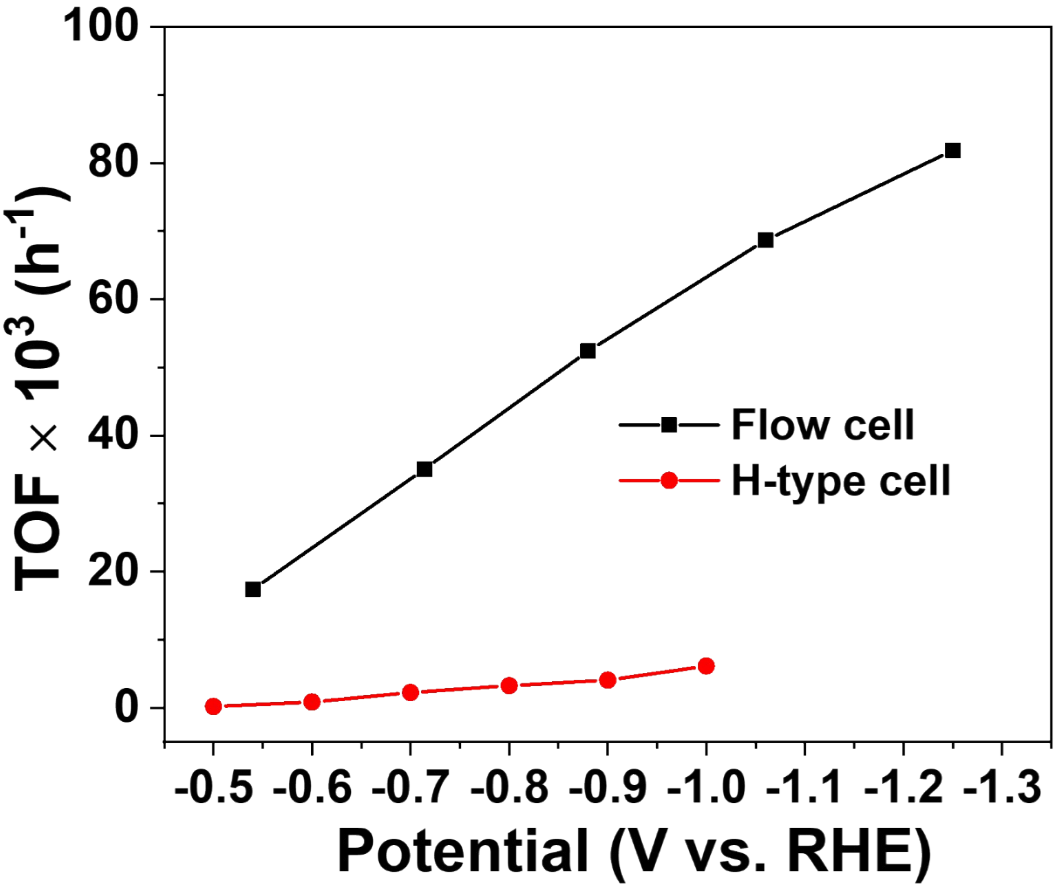

Fig. S22 Comparison TOF of CMPANI-3 in flow cell with that in H-type cell.

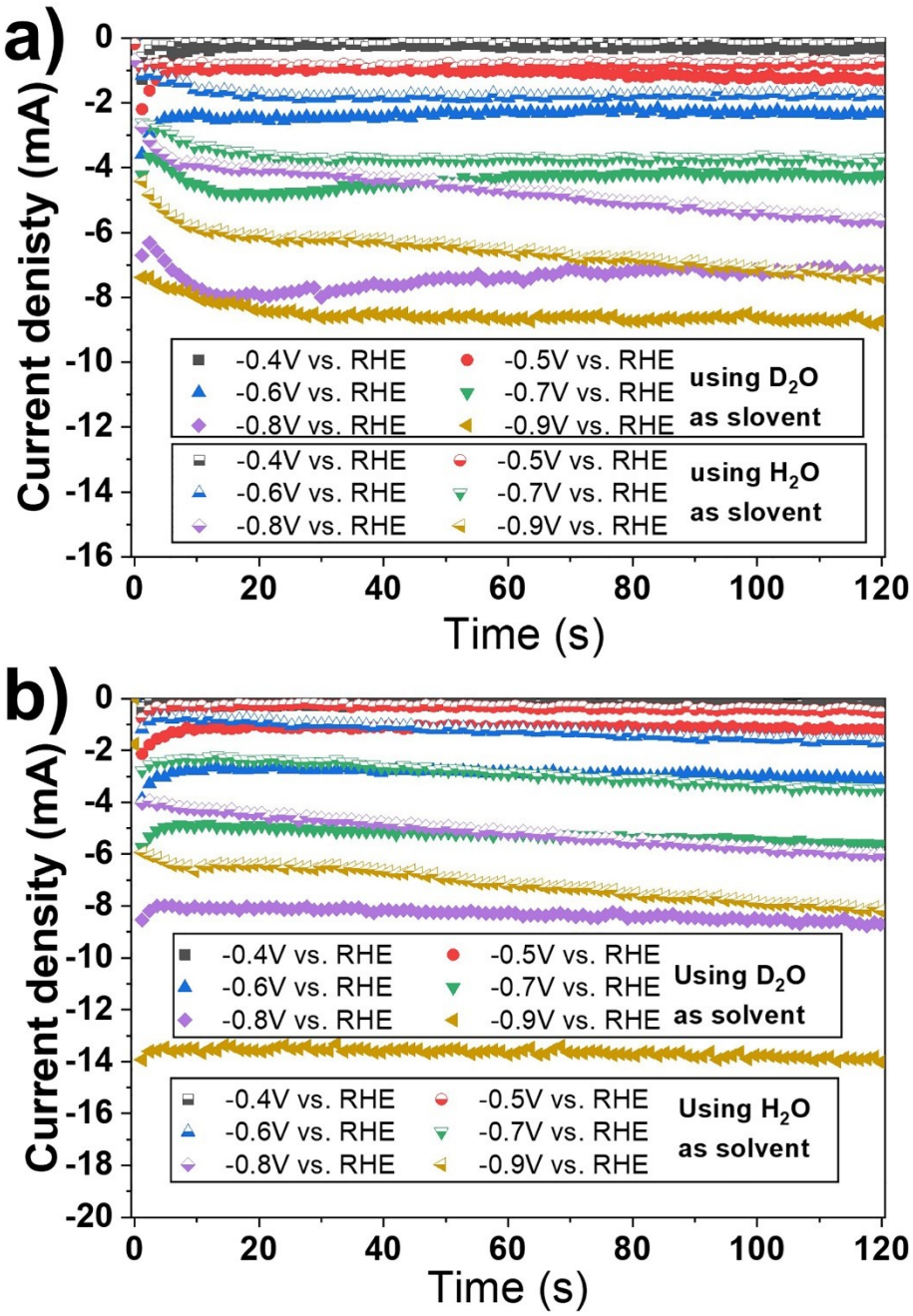

Fig. S23 Current densities of CMPANI-1 (a) and CMPANI-3 (b) at different potentials for 120 s, using D_2O and H_2O as solvent, respectively.

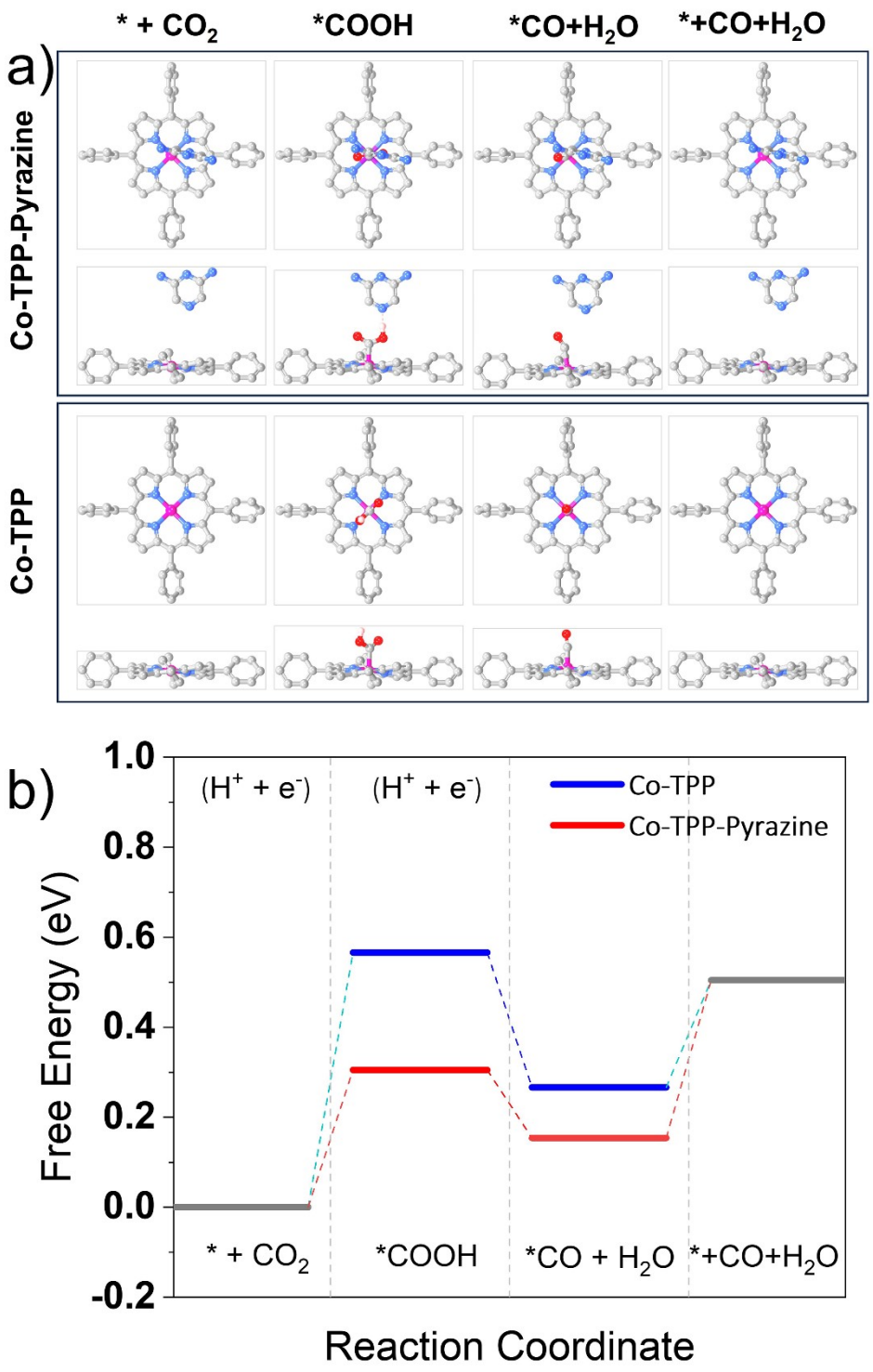

Fig. S24 a) DFT-calculated models and b) free energy of catalytic sites of CMPANI-3 and Co-TPP in different CO_2RR steps

3. Tables

Table S1. Element contents of CMPANI-n

Samples	Theoretical calculations (wt%)			Test results [a] (wt%)			Pd [b] (10^2 ×wt%)	Co [b] (wt%)
	C	N	Co	C	N	Co		
CMPANI-1	80.56	12.74	6.70	86.37	9.55	4.08	2.54	5.17
CMPANI-2	77.41	15.88	6.68	81.86	13.23	4.91	2.71	5.10
CMPANI-3	74.31	19.02	6.67	81.10	14.80	4.09	2.19	4.98

a) obtained by XPS analysis; b) obtained by ICP-MS measurement

Table S2. Best fitting EXAFS data for CMPANI-3

Sample	Shell	N	R (Å)	σ^2 (10^{-3} Å^2)	R factor
CMPANI-3	Co-N	4 (fixed)	1.94	2.5	0.02

Table S3. The electrochemical data of CMPANI-n

Samples	LUMO (eV)[a]	HOMO (eV)[b]	$E_{g(opt)}$ (eV)[c]	$LUMO_{Cal}$ (eV)[d]	$HOMO_{Cal}$ (eV)[d]	$E_{g,Cal}$ (eV)[d]
CMPANI-1	−3.42	−4.76	1.34	−1.79	−4.57	2.78
CMPANI-2	−3.45	−4.66	1.21	−1.73	−4.55	2.82
CMPANI-3	−3.46	−4.65	1.19	−1.64	−4.32	2.68

[a] LUMO = HOMO + $E_{g(opt)}$. [b] measured by UPS. [c] Band gaps determined from the UV-Vis absorption spectra. [d] Calculated HOMO/LUMO levels based on DFT simulation

Table S4. Comparison of electrocatalytic CO_2 reduction performance of our catalyst with current state-of-art CMP-based catalysts in H-type cell

Catalysts	Electrolyte	*j*/mA cm^{-2}	V vs RHE	Main products (FE_{CO})	TOF (h^{-1})	Ref.
CMPANI-3	**0.5 M $KHCO_3$**	**-3.7**	**−0.6**	**94%**	**861**	**This work**
		-7.5	**−0.7**	**97%**	**2264**	
		-11.4	**−0.8**	**96%**	**3262**	
PorCo-MOF	0.1 M $KHCO_3$	-1	−0.6	76%	200	Ref. 2
COF-367-PorCo(1%)	0.5 M $KHCO_3$	-0.4	−0.55	90%	764	Ref. 3
PorCo-TTF COF	0.5 M $KHCO_3$	-3	−0.7	91.3%	4608	Ref. 4
PorCo-B18C6 COF	0.5 M $KHCO_3$	-3	−0.7	93.3%	696	Ref. 5
TT-PorCo COF	0.5 M $KHCO_3$	-7.28	−0.7	86%	481	Ref. 6
CoP-BDT_{HexO} COF	0.5 M $KHCO_3$	-5.2	−0.77	97.6%	4506	Ref. 7
CoP-BDT-COF		-2.9	−0.77	96%	2468	
CoCoPCP	0.5 M $KHCO_3$	-8	−0.55	94%	360	Ref. 8
CoPor-N3	0.5 M $KHCO_3$	-14	−0.5	96%	550	Ref. 9
p(CoPc-1)	0.5 M $KHCO_3$	-1.1	−0.99	84%	450	Ref. 10
PorNi-CTF	0.5 M $KHCO_3$	-52.9	−0.9	97%	1692	Ref. 11

Table S5. Performance of CMPANI-3 comparison with reported work for CO_2-to-CO electrocatalysts in flow cell

Catalysts	Electrolyte	*j*/mA cm^{-2}	V vs RHE	(FE_{co})	Ref.
CMPANI-3	**1M KOH**	**50**	**−0.54**	**93.8**	**This work**
		100	**−0.71**	**94.5**	
		150	**−0.88**	**94.2**	
		200	**−1.06**	**92.6**	
		250	**−1.25**	**88.3**	
CoPc2	1 M KOH	175	−0.9	94	Ref. 12
CoPc + phenol	1 M KOH	200	−1.58	89	Ref. 13
CoTAPc	1 M KOH	250	−0.7	95	Ref. 14
Hg-CoTPP	1 M KOH	250	−0.64	99	Ref. 15
N-CoMe2Pc	1 M KOH	150	−1.0	62.4	Ref. 16
EP-CoPor	1 M KOH	220	−0.7	98	Ref. 17
Au-C	1 M KOH	100	−0.5	91.8	Ref. 18
Ag	1 M KOH	100	−1.97	96	Ref. 19

4. References

1. J. Kang, M. Wang, C. Lu, C. Ke, P. Liu, J. Zhu, F. Qiu and X. Zhuang, *Materials*, **2020**, *13*, 1513.
2. N. Kornienko, Y. Zhao, C. S. Kley, C. Zhu, D. Kim, S. Lin, C. J. Chang, O. M. Yaghi and P. Yang, *J. Am. Chem. Soc.*, **2015**, *137*, 14129-14135.
3. S. Lin, C. S. Diercks, Y.-B. Zhang, N. Kornienko, E. M. Nichols, Y. Zhao, A. R. Paris, D. Kim, P. Yang, O. M. Yaghi and C. J. Chang, *Science*, **2015**, *349*, 1208-1213.
4. H.-J. Zhu, M. Lu, Y.-R. Wang, S.-J. Yao, M. Zhang, Y.-H. Kan, J. Liu, Y. Chen, S.-L. Li and Y.-Q. Lan, *Nat. Commun.*, **2020**, *11*, 497.
5. S. An, C. Lu, Q. Xu, C. Lian, C. Peng, J. Hu, X. Zhuang and H. Liu, *ACS Energy Lett.*, **2021**, *6*, 3496-3502.
6. Q. Wu, M.-J. Mao, Q.-J. Wu, J. Liang, Y.-B. Huang and R. Cao, *Small*, **2021**, *17*, 2004933.
7. T. He, C. Yang, Y. Chen, N. Huang, S. Duan, Z. Zhang, W. Hu and D. Jiang, *Adv. Mater.*, **2022**, *34*, 2205186.
8. T. Wang, L. Xu, Z. Chen, L. Guo, Y. Zhang, R. Li and T. Peng, *Appl. Catal. B-Environ.*, **2021**, *291*, 120128.
9. T. Wang, L. Guo, H. Pei, S. Chen, R. Li, J. Zhang and T. Peng, *Small*, **2021**, *17*, 2102957.
10. J. Luangchaiyaporn, D. Wielend, D. Solonenko, H. Seelajaroen, J. Gasiorowski, M. Monecke, G. Salvan, D. R. T. Zahn, N. S. Sariciftci and P. Thamyongkit, *Electrochim. Acta*, **2021**, *367*, 137506.
11. C. Lu, J. Yang, S. Wei, S. Bi, Y. Xia, M. Chen, Y. Hou, M. Qiu, C. Yuan, Y. Su, F. Zhang, H. Liang and X. Zhuang, *Adv. Funct. Mater.*, **2019**, *29*, 1806884.
12. M. Wang, K. Torbensen, D. Salvatore, S. Ren, D. Joulié, F. Dumoulin, D. Mendoza, B. Lassalle-Kaiser, U. Işci, C. P. Berlinguette and M. Robert, *Nat. Commun.*, **2019**, *10*, 3602.

13. S. Ren, D. Joulié, D. Salvatore, K. Torbensen, M. Wang, M. Robert and C. P. Berlinguette, *Science*, **2019**, *365*, 367-369.
14. J. Su, J.-J. Zhang, J. Chen, Y. Song, L. Huang, M. Zhu, B. I. Yakobson, B. Z. Tang and R. Ye, *Energy Environ. Sci.*, **2021**, *14*, 483-492.
15. M. Fang, L. Xu, H. Zhang, Y. Zhu and W.-Y. Wong, *J. Am. Chem. Soc.*, **2022**, *144*, 15143-15154.
16. M. Li, C. Yan, R. Ramachandran, Y. Lan, H. Dai, H. Shan, X. Meng, D. Cui, F. Wang and Z.-X. Xu, *Chem. Eng. J.*, **2022**, *430*, 133050.
17. C. Wang, Y. Chen, D. Su, W.-L. Man, K.-C. Lau, L. Han, L. Zhao, D. Zhan and X. Zhu, *Adv. Mater.*, **2023**, *35*, 2303179.
18. R. Shi, J. Guo, X. Zhang, G. I. N. Waterhouse, Z. Han, Y. Zhao, L. Shang, C. Zhou, L. Jiang and T. Zhang, *Nat. Commun.*, **2020**, *11*, 3028.
19. R. B. Kutz, Q. Chen, H. Yang, S. D. Sajjad, Z. Liu and I. R. Masel, *Energy Technol.*, **2017**, *5*, 929-936.